Editors' Suggestion

Magnetic inhomogeneities in the quadruple perovskite manganite $[Y_{2-x}Mn_x]Mn_6O_{12}$

A. M. Vibhakar,[1,2,*] D. D. Khalyavin,[3] P. Manuel,[3] N. J. Steinke,[4] L. Zhang,[5,6] K. Yamaura,[5,6] A. A. Belik,[5] and R. D. Johnson[7]

[1]*Clarendon Laboratory, Department of Physics, University of Oxford, Oxford OX1 3PU, England, United Kingdom*
[2]*Diamond Light Source, Ltd, Harwell Science and Innovation Campus, Didcot, Oxfordshire OX11 0DE, England, United Kingdom*
[3]*ISIS Facility, Rutherford Appleton Laboratory–STFC, Chilton, Didcot OX11 0QX, England, United Kingdom*
[4]*Institut Laue-Langevin, 71 Avenue des Martyrs, F-38042 Grenoble, France*
[5]*Research Center for Materials Nanoarchitectonics, National Institute for Materials Science, Namiki 1-1, Tsukuba, Ibaraki 305-0044, Japan*
[6]*Graduate School of Chemical Sciences and Engineering, Hokkaido University, North 10 West 8, Kita-ku, Sapporo, Hokkaido 060-0810, Japan*
[7]*Department of Physics and Astronomy, University College London, Gower Street, London WC1E 6BT, England, United Kingdom*

(Received 8 May 2023; revised 5 July 2023; accepted 11 July 2023; published 3 August 2023)

A combination of competing exchange interactions and substitutional disorder gives rise to magnetic inhomogeneities in the $[Y_{2-x}Mn_x]Mn_6O_{12}$ $x = 0.23$ and 0.16 quadruple perovskite manganites. Our neutron powder scattering measurements show that both the $x = 0.23$ and 0.16 samples separate into two distinct magnetic phases; below $T_1 = 120 \pm 10$ K the system undergoes a transition from a paramagnetic phase to a phase characterized by short-range antiferromagnetic clusters contained in a paramagnetic matrix, and below $T_2 \approx 65$ K the system is composed of well-correlated long-range collinear ferrimagnetic order, punctuated by short-range antiferromagnetic clusters. A sharp increase in the antiferromagnetic phase fraction is observed below ≈ 33 K, concomitant with a decrease in the ferrimagnetic phase fraction. Our results demonstrate that the theoretically proposed antiferromagnetic phase is stabilized in the $[Y_{2-x}Mn_x]Mn_6O_{12}$ manganites in the presence of dominant *B-B* exchange interactions, as predicted.

DOI: 10.1103/PhysRevB.108.054403

I. INTRODUCTION

Competing exchange interactions and disorder are two parameters that can be tuned to access a wide range of macroscopically distinct magnetic phases. For instance, disordered magnetic phases such as spin glasses arise from the presence of strong quenched disorder and competing exchange interactions, while unordered magnetic systems, such as spin liquids, typically arise from strong competing exchange and occur in the absence of quenched disorder. Competing exchange and disorder also form essential ingredients for realizing Griffiths phases [1], which occur in magnetic systems when clusters of magnetic order form that are large enough to produce a singularity in the free energy [2–4]. Imaging and understanding the mathematical properties of such magnetic phases has shaped our understanding of neural networks [5] and complex matter [6], and continues to play an important role in demonstrating novel forms of complex behavior [6].

An exemplary family of materials that demonstrate the interplay between disorder and competing exchange is that of the simple perovskite manganites. In the absence of any substitutional disorder, i.e., for $A^{3+}MnO_3$, well-ordered antiferromagnetic (AFM) ground state structures are stabilized. The introduction of hole doping, through the substitution of a divalent cation on the *A* sites, gives rise to an electronic texture that is inhomogeneous on the nanoscale. In general for $A(III)_{1-x}A'(II)_xMnO_3$ $x < 0.5$, an insulator to metal phase transition is observed below T_C (Curie temperature), and the system is observed to order ferromagnetically in the metallic phase owing to the double exchange mechanism [7]. Numerous studies have found that there is a finite temperature interval that precedes the phase transition to ferromagnetic (FM) order, where the system is characterized by coexistence of paramagnetic insulating and FM metallic regions, a Griffiths phase [8,9]. Here, charge doping causes the separation of these systems into the two distinct electronic phases, giving rise to the two magnetic phases and the establishment of a Griffiths phase. Furthermore for certain compositions of the mixed valence manganites [10], such as in $Pr_{0.7}Ca_{0.3}MnO_3$ [11], the randomly dispersed Mn^{4+} on the *B*-site sublattice gives rise to short-range metallic and insulating charge ordered regions below T_C, which order ferromagnetically and antiferromagnetically respectively. The localization of the charge in the insulating regions and the corresponding orbital order give rise to antiferromagnetism as understood through the context of the Goodenough-Kanamori-Anderson rules [12]. The coexistence of the two electronically and magnetically ordered phases in the simple perovskite manganites is argued to be directly responsible for establishing colossal magnetoresistance [10,13–16], although this has yet to be proven [17,18].

A similar picture is emerging in the columnar ordered quadruple perovskite manganites; competing exchange

*Corresponding author: anuradha.vibhakar@diamond.ac.uk

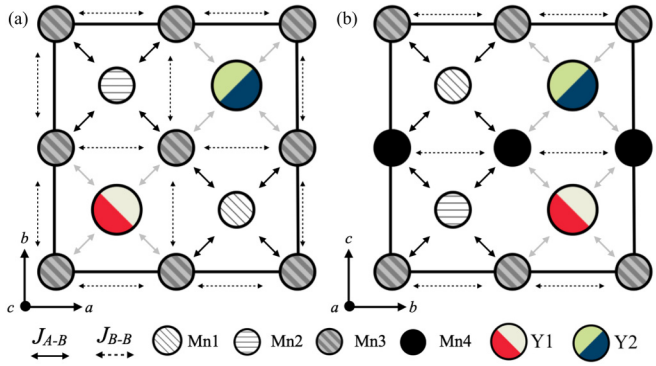

FIG. 1. Selected slices through the unit cell of $[Y_{2-x}Mn_x]Mn_6O_{12}$ as projected from the (a) c axis ($0.5 \leqslant z \leqslant 1$) and the (b) a axis ($0.5 \leqslant x \leqslant 1$) showing the Mn1, Mn2, Mn3, Mn4, Y1, and Y2 ions and the A-B and B-B exchange interactions. The oxygen ions are omitted for clarity. The *Pmmn* unit cell is shown by the solid black line. The competing exchange interactions, $J_{A\text{-}B}$ and $J_{B\text{-}B}$ are shown by the black solid and dashed arrows respectively. Th solid gray arrow indicates an A-B exchange interaction that switches on when Mn substitutes Y on that site. Note the $J_{B\text{-}B}$ is approximated to be the same for the Mn3 and Mn4 ions, and along a and b for simplicity.

interactions and substitutional disorder are giving rise to a number of microscopically distinct magnetic phases. In the $A_2A'A''B_4O_{12}$ (B = Mn) manganites the competing B-B and A-B exchange interactions, shown in Fig. 1, have thus far given rise to well-correlated magnetic structures on average. For instance in $Tm_2MnMnMn_4O_{12}$ and $Sm_2MnMnMn_{4-x}Ti_xO_{12}$ a long-range ordered collinear ferrimagnetic (FIM) phase was observed [19,20]. It was suggested that the system ordered on average to favor the exchange interactions of the greatest strength, A-B exchange, while the competing exchange interactions, AFM B-B exchange, manifested as spin fluctuations reducing the measured moment. Similarly in $R_2CuMnMn_4O_{12}$(R = Y or Dy), well-correlated magnetic phases were observed, including the collinear FIM order stable in intermediate temperature range [21]. However, owing to a reduction in the A-B exchange interactions, B-B exchange was accommodated by spin canting onto the B-site layers.

In this paper we show that the introduction of substitutional disorder on the A sites in the presence of the competing exchange interactions causes $[Y_{2-x}Mn_x]Mn_6O_{12}$ $x = 0.23$ and 0.16 to separate into two distinct magnetic phases: a collinear FIM phase that is favored by A-B exchange, and an AFM phase favored by B-B exchange. In analogy to the introduction of *charge* doping in the simple perovskite manganites, the introduction of *spin* doping through the substitution of magnetic Mn ions for nonmagnetic Y^{3+} gives rise to a spin texture that is inhomogeneous on the nanoscale. In these systems we have observed the formation of short-range AFM clusters contained in a paramagnetic matrix between T_1 and T_2. Below T_2, a phase transition to well-correlated long-range FIM order was observed, which coexists with the short-range AFM clusters. A sharp increase in the AFM phase fraction was observed below $\approx$33 K, concomitant with a decrease in the FIM phase fraction. We note that characterizing such effects of spin doping is of significance, given recent trends to replace established electronic paradigms with spin-only functionality in future spintronic devices.

II. EXPERIMENTAL DETAILS

$Y_{1.840(7)}Mn_{0.160(8)}Mn_6O_{12}$($x = 0.16$) and $Y_{1.768(9)}Mn_{0.232(9)}Mn_6O_{12}$ ($x = 0.23$) powder samples were made from stoichiometric mixtures of Mn_2O_3 and Y_2O_3 (99.9%) using a high-temperature high-pressure synthesis method as detailed in Ref. [22]. DC magnetization measurements were performed on the samples using a superconducting quantum interference device magnetometer (Quantum Design, MPMS-XL-7T) between 2 and 400 K under both zero-field-cooled and field-cooled on cooling (FCC) conditions. Time of flight neutron powder-diffraction (NPD) measurements were performed on 1.93 g of the $x = 0.23$ sample and 1.51 g sample of the $x = 0.16$ sample using the WISH diffractometer at ISIS [23]. Data with high counting statistics were collected at 1.5 and 85 K for both samples—temperatures representative of each of the magnetically ordered phases. Data with lower counting statistics were collected for both samples on warming between 1.5 and 85 K in 2- and 5-K steps, between 90 and 140 K in 10-K steps, and at 200 and 250 K. Small angle neutron scattering (SANS) measurements were performed on D33 at the Institute Laue Langevin. Each of the samples listed above was pressed into a flat disk like pellet, and placed in an aluminium sample mount. Data were collected in a single detector setting for both samples ($0.003 \leqslant Q \leqslant 0.1$ Å^{-1} and $\Delta Q = 0.0005$ Å^{-1}), and at temperatures between 300 and 5 K. Field dependent SANS measurements were performed on the $x = 0.23$ sample with the magnetic field applied parallel to the incoming neutron beam, and data were collected at 5, 90, and 130 K using fields of 0.01, 0.1, and 0.5 T.

III. RESULTS

A. Neutron powder-diffraction data

The published *Pmmn* crystal structure model [22] was used to refine the NPD data collected in the paramagnetic phase, at 250 K for the $x = 0.16$ sample and 255 K for the $x = 0.23$ sample, as shown in Figs. 2(a) and 2(b) respectively. The A sites (labeled Y1 and Y2) were predominately occupied by nonmagnetic Y^{3+} and a small amount of magnetic Mn ions. The degree of cation disorder on these sites is what differentiates the two samples. As discussed later we show that it has profound implications for tuning exchange interactions, as it in effect leads to spin doping of the A sublattice [24]. The A sites were occupied by Mn^{3+} in a square planar coordination (labeled Mn1) and the A' sites by Mn^{2+} in a tetrahedral coordination (labeled Mn2). The two symmetry inequivalent B sites, labeled Mn3 and Mn4, form ab layers composed of Mn^{3+} and $Mn^{3.5+}$ ions respectively, that stack alternately along c. The refined stoichiometries of the two $Y_2Mn_6O_{12}$ samples were $Y_{1.768(9)}Mn_{0.232(9)}Mn_6O_{12}$ and $Y_{1.840(7)}Mn_{0.160(8)}Mn_6O_{12}$. Both samples contained a YMn_2O_5 impurity, with a weight fraction of 1.26 and 1.32 wt. % respectively. The $x = 0.16$ sample also contained a $YMnO_3$

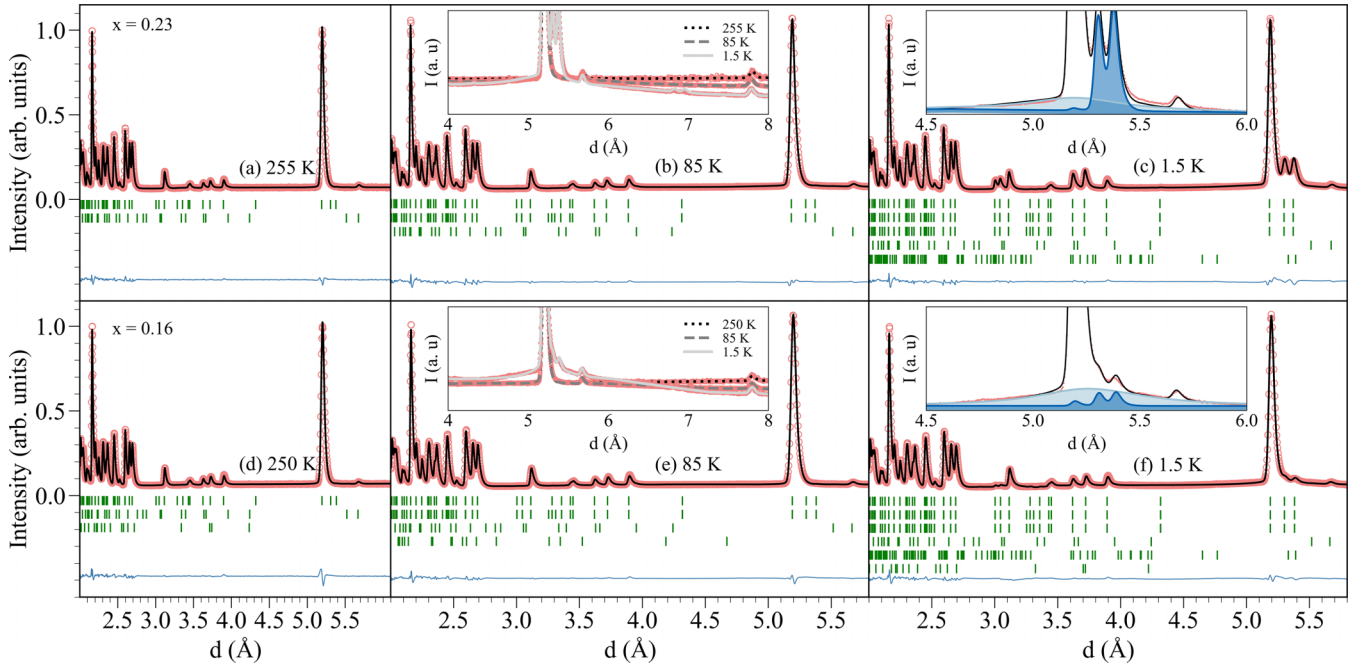

FIG. 2. Neutron powder-diffraction data collected on the time-of-flight diffractometer WISH at ISIS at temperatures representative of the paramagnetic and two magnetically ordered phases of (a)–(c) $x = 0.23$ and (d)–(f) $x = 0.16$ $[Y_{2-x}Mn_x]Mn_6O_{12}$. The insets in (b) and (e) compare the NPD patterns at either 250 or 255 K, 85 K, and 1.5 K for each of the samples. The insets in (c) and (f) show the contributions of the AFM phase and FIM phase to the {110} family of reflections, given by the light and dark blue shaded regions respectively for the diffraction pattern collected at 1.5 K. The data are represented by the red circles and the fit of the data is represented by the black or gray lines. The green tick marks represent the nuclear and magnetic reflections of the main and any impurity phases. The reflections labeled (1) are from the main $[Y_{2-x}Mn_x]Mn_6O_{12}$ phase, those labeled (2) are from the YMn_2O_5 impurity, and those labeled (3) are from the $YMnO_3$ impurity.

impurity, with a weight fraction of 0.37 wt. %. An excellent fit was achieved for both samples, $R = 3.30\%$, $wR = 3.30\%$, and $R_{\text{Bragg}} = 3.04\%$ for $x = 0.23$ at 250 K and $R = 3.36\%$, $wR = 3.71\%$, and $R_{\text{Bragg}} = 3.02\%$ for $x = 0.16$ at 255 K. The refined crystal structure parameters are given in Tables III and IV.

As the temperature was lowered below 200 K, three distinct changes were observed to the NPD pattern of both samples. First, between 200 and 120 K the paramagnetic background gradually decreased [see insets of Figs. 2(b) and 2(e)], but no additional intensity was observed across the rest of the patterns. Second, between 130 and 110 K broad diffuse intensity started to appear centered about the {110} and {112} families of reflections [inset of Figs. 2(c) and 2(f)], which steadily grew till $\approx$33 K, before rapidly increasing till the lowest measured temperatures. It was not possible to pinpoint the exact onset temperature of the broad diffuse magnetic intensity and therefore an approximate value of 120 ± 10 K will be given for T_1 in the rest of the paper. Third, below T_2, which was 67 K for the $x = 0.23$ sample and 64 K for the $x = 0.16$ sample, well-correlated intensity appeared at the (011), (101), (121), (211), (020), and (200) Bragg reflections (Fig. 2). The intensity of these Bragg reflections was significantly higher for the $x = 0.23$ than the $x = 0.16$ sample, and grew till $\approx$33 K, before steadily decreasing till the lowest measured temperatures.

The intensity that appeared below T_2 was identified to be magnetic in origin as the magnetic susceptibility measured on the sample underwent a rapid increase at T_2, indicative of the ordering of a FM or FIM phase. The broad diffuse intensity that was observed to appear below T_1 was also identified to have a magnetic origin given that it directly competes with the sharp well-correlated magnetic intensity below 33 K. Details of whether a signature of a phase transition at T_1 is observed in magnetometry or specific heat capacity is discussed further in Sec. III C and Appendix 5 respectively.

As all the magnetic intensity was observed on top of structural reflections, the magnetic ordering was determined to transform by a Γ-point irreducible representation. The magnetic Γ-point representation decomposes into seven irreducible representations, determined using the ISOTROPY software suite, and which are given in terms of the symmetry-adapted magnetic modes, F_i, A_i, X_i, and Y_i, defined in Appendix 2a. Structure factors were calculated for each of the symmetry adapted basis modes (Appendix 2c), and the results are summarized in Table I for relevant reflections. These structure factor calculations show that the magnetic intensity observed below T_2 on the (020) and (200) reflections can originate from either *A*- or *B*-site FM F_i modes (Table I). The observation of equal amounts of magnetic intensity on the (200) and (020) reflections and zero magnetic intensity on the (002) reflections is consistent with the ordering of F_z modes, which transform by the Γ_2^+ irrep. Magnetic structure models were constructed by taking linear combinations of the symmetry adapted basis functions of the Γ_2^+ irrep, and refined against the NPD data using the FULLPROF software

TABLE I. Reflection conditions for B-site F_i, A_i, X_i, and Y_i symmetry adapted basis modes as determined by structure factor calculations shown in Appendix 2c. When two B-site modes are listed, the first mode corresponds to the magnetic ordering of the Mn3 layer, and the second mode corresponds to the magnetic ordering of the Mn4 layer. For instance the notation $A_iA_{\bar{i}}$ equates to the Mn3 ions transforming by an A_i mode and the Mn4 ions transforming by an $A_{\bar{i}}$ mode, where the barred subscript implies the Mn4 sublattice is antialigned with respect to Mn3. f_m is the magnetic form factor, which is approximated to be the same for the Mn3 and Mn4 ions. Note that the direction of the magnetic moment has not been taken into account when calculating the structure factors.

Mode	(001)	{200}	(010)	(100)	(011)	(101)	(110)	(111)	(012)	(102)	(112)	(121)	(211)
							A sites						
F_i	0	$2f_m$	0	0	$2f_m$	$2f_m$	$2f_m$	0	0	0	$2f_m$	$2f_m$	$2f_m$
A_i	$2f_m$	0	$2f_m$	$2f_m$	0	0	0	$2f_m$	$2f_m$	$2f_m$	0	0	0
							B sites						
F_iF_i	0	$8f_m$	0	0	0	0	0	0	0	0	0	0	0
$F_iF_{\bar{i}}$	$8f_m$	0	0	0	0	0	0	0	0	0	0	0	0
F_i	$4f_m$	$4f_m$	0	0	0	0	0	0	0	0	0	0	0
A_iA_i	0	0	0	0	0	0	$8f_m$	0	0	0	$8f_m$	0	0
$A_iA_{\bar{i}}$	0	0	0	0	0	0	0	$8f_m$	0	0	0	0	0
A_i	0	0	0	0	0	0	$4f_m$	$4f_m$	0	0	$4f_m$	0	0
X_iX_i	0	0	0	$8f_m$	0	0	0	0	0	$8f_m$	0	0	0
$X_iX_{\bar{i}}$	0	0	0	0	0	$8f_m$	0	0	0	0	0	$8f_m$	0
X_i	0	0	0	$4f_m$	0	$4f_m$	0	0	0	$4f_m$	0	$4f_m$	0
Y_iY_i	0	0	$8f_m$	0	0	0	0	0	$8f_m$	0	0	0	0
$Y_iY_{\bar{i}}$	0	0	0	0	$8f_m$	0	0	0	0	0	0	0	$8f_m$
Y_i	0	0	$4f_m$	0	$4f_m$	0	0	0	$4f_m$	0	0	0	$4f_m$

suite. The magnetic structure model that gave the best fit to the sharp magnetic Bragg peaks at 40 K, where a smoothly varying background was used to fit the broad diffuse magnetic intensity, was one in which the Mn1, Mn2, Mn3, and Mn4 sublattices order with F_z modes. The Mn2 sublattice moments were oriented antiparallel to the Mn1, Mn3, and Mn4 sublattice moments to give a net collinear FIM structure as shown in Fig. 3, similar to both magnetically ordered phases of $Tm_2MnMnMn_4O_{12}$ [19] and all three magnetically ordered phases of $R_2CuMnMn_4O_{12}$ (R = Y or Dy) [21]. This magnetic structure solution is consistent with the rapid increase of the susceptibility measured below T_2, as discussed in further detail in Sec. III C.

The diffuse magnetic intensity centered about the {110} and {112} reflections, observed to appear below T_1, could have originated from AFM B-site modes or F_i A-site modes coupled antiferromagnetically (see Table II and Appendix 2c for further details). As these A- and B-site modes originate in different irreps, it is unlikely that both sublattices contributed to the diffuse intensity, and owing to the broadness of the diffuse intensity it was impossible to distinguish which of these two sets of modes contributed to the NPD data. Instead SANS measurements confirmed the absence of any FM ordering between T_1 and T_2, as detailed in Sec. III B, confirming that the diffuse intensity originates in AFM modes at the B sites.

The AFM B-site modes that can scatter at the {110} and {112} reflections are the A_iA_i, $X_iX_{\bar{i}}$, and $Y_iY_{\bar{i}}$ modes [25], as shown in Table I. Each of these three B-site AFM mode combinations was tested against the NPD data, where the amplitudes of the modes on the Mn3 and Mn4 layer were constrained to be the same. The best fit to the diffuse intensity was using a magnetic structure model in which the

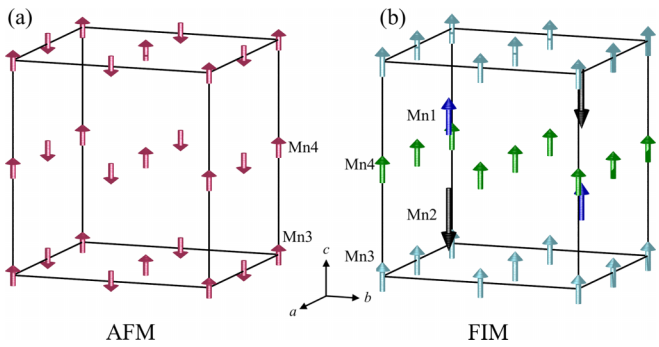

FIG. 3. Experimentally determined magnetic structure of (a) the AFM phase and (b) the FIM phase of the $x = 0.23$ sample of $[Y_{2-x}Mn_x]Mn_6O_{12}$ at 1.5 K.

TABLE II. Moment magnitudes and phase fractions (P.F.) refined at 1.5 K for the $x = 0.23$ and 0.16 samples for the AFM and FIM phases for each of the symmetry inequivalent magnetic sublattices, under the assumption that the B-site moments are of the same magnitude in the AFM and FIM phases at 1.5 K.

	Mn1	Mn2	Mn3	Mn4	P.F.
			$x = 0.23$		
FIM	2.5(2)	−4.0(2)	1.8(3)	1.7(3)	0.4(2)
AFM			1.8(3)	1.7(3)	0.6(2)
			$x = 0.16$		
FIM	2.4(7)	−1.8(7)	1.6(3)	1.5(4)	0.14(6)
AFM			1.6(3)	1.5(4)	0.86(6)

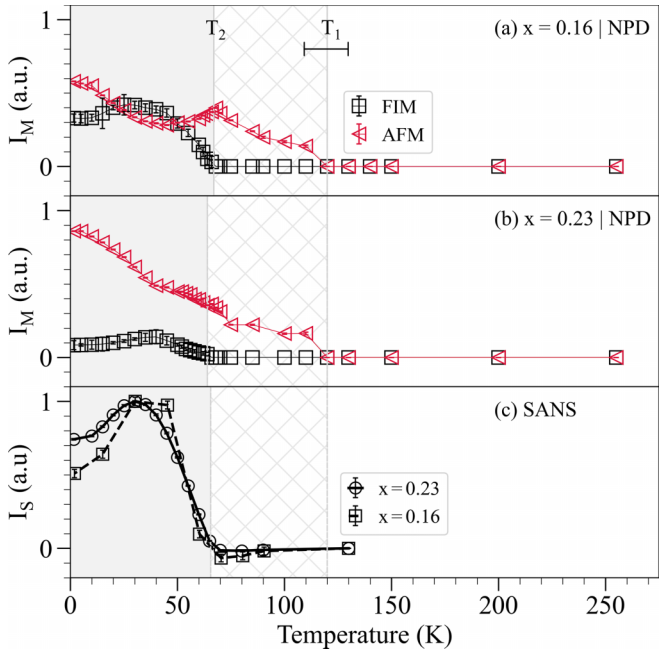

FIG. 4. I_M represents the average temperature evolution of magnetic scattering intensity from each phase for the (a) $x = 0.23$ and (b) $x = 0.16$ samples. I_M can be taken to indicate the evolution of the magnetic moments squared, scaled by their respective phase fraction. (c) Temperature dependence of the normalized magnetic SANS intensity for the $x = 0.23$ and $x = 0.16$ samples. The grey solid and hatched regions correspond to the temperature regions $T < T_2$ and $T_2 \leqslant T \leqslant T_1$. The uncertainty on T_1 is indicated by a horizontal error bar.

B-site magnetic structure transforms by an A_zA_z mode (Γ_1^+ irrep) to give an AFM structure, shown in Fig. 3. Fitting the diffuse intensity centered at the {110} family of reflections with a Lorentzian function, we extracted a correlation length of ≈150 Å, which one can take as being indicative of the extent of the short-range AFM order [26].

The above magnetic structure models were used to simultaneously fit the NPD data; the AFM structure was used to fit the broad diffuse scattering and the FIM structure to fit the sharp Bragg peaks. Since there is 100% correlation between the moment size and the phase fraction, it was not possible to get these two quantities separately for the AFM and FIM phases without any additional constraints. The unconstrained refinement can only provide information about the moment size scaled by the respective phase fraction. Thus, the integrated intensities of the AFM and FIM magnetic reflections as a function of temperature also represent temperature evaluation of the scaled moments (squared) and not the absolute moment size as in the case of a single magnetic phase. To emphasize this fact, we call these intensities as average magnetic scattering intensities, I_M, and their temperature evolution is shown in Fig. 4. In addition to the phase transitions discussed above, one can observe that below ≈33 K, the average magnetic intensity scattered from the FIM phase begins to decrease, which occurs concomitantly with an increase in the scattered intensity from the AFM phase. By assuming the *B*-site moments were of the same magnitude in the AFM and FIM phases at 1.5 K, the moment magnitudes of all relevant sublattices and phase fractions of the AFM and FIM phases were refined, as given in Table II. The model gave a very good fit to the data, $R_{\text{Mag}} = 3.04\%$ for the $x = 0.23$ sample and $R_{\text{Mag}} = 7.39\%$ for the $x = 0.16$ sample at 1.5 K. Note that the larger value of R_{Mag} for the $x = 0.16$ sample is owing to the weak intensity that was scattered from the FIM phase. The phase fraction of the FIM phase was larger in the $x = 0.23$ sample compared with the $x = 0.16$ sample, consistent with our qualitative observations described above.

B. Small angle neutron scattering

SANS measurements were performed to determine whether the broad diffuse scattering measured below T_1 originated from AFM or FM order. The magnetic scattering length density from SANS is given by the average magnetic moment in a unit cell, which is zero for AFM order, and hence the presence of finite SANS intensity is indicative of FM or FIM ordering.

The transmitted intensity from the full beam and the scattered intensity from an empty sample cell were used to normalize the SANS patterns so that any contributions from the transmitted beam and aluminium sample holder were subtracted away. The SANS pattern collected at room temperature was also subtracted to remove the nuclear contribution to the scattered intensity. Figure 4(c) shows the variation in the magnetic SANS intensity summed over the collected Q range and plotted as a function of temperature for both samples. No SANS intensity was observed between T_1 and T_2 of either sample, indicating the absence of any FM clusters in this temperature region. Furthermore, in the presence of any FM clusters, one would expect the application of a magnetic field to couple to the net magnetization of the cluster and cause a change to the magnetic SANS intensity, as has been observed in other systems [1]. No change to the SANS intensity was observed between T_1 and T_2 under applied magnetic fields of up to 0.5 T, as shown in Fig. 7, confirming the absence of any FM order.

The magnetic SANS intensity that begins to appear below T_2 in both samples [Fig. 4(c)] reproduces the observed variation in intensity of the Bragg peaks measured from NPD. Hence, we assign this SANS intensity to the onset of the FIM phase, which is expected to scatter at the (0,0,0) reflection, the tail of which is observed in the SANS data.

C. DC susceptibility measurements

Between 400 and 250 K the inverse susceptibility follows a Curie-Weiss-like temperature dependence, as shown in Figs. 5(c) and 5(d), with a Curie-Weiss temperature of −65 K for the $x = 0.23$ sample and −89 K for the $x = 0.16$ sample. Between 200 K and T_1 a departure from Curie-Weiss-like behavior was observed—there was a slight curvature to the inverse susceptibility. Taken together with the decrease in the paramagnetic background of the NPD patterns at these temperatures, this suggests the onset of short-range magnetic correlations.

A downturn in the inverse susceptibility was observed between T_2 and 110 K, shown in Figs. 5(e) and 5(f), and is suppressed upon application of a magnetic field.

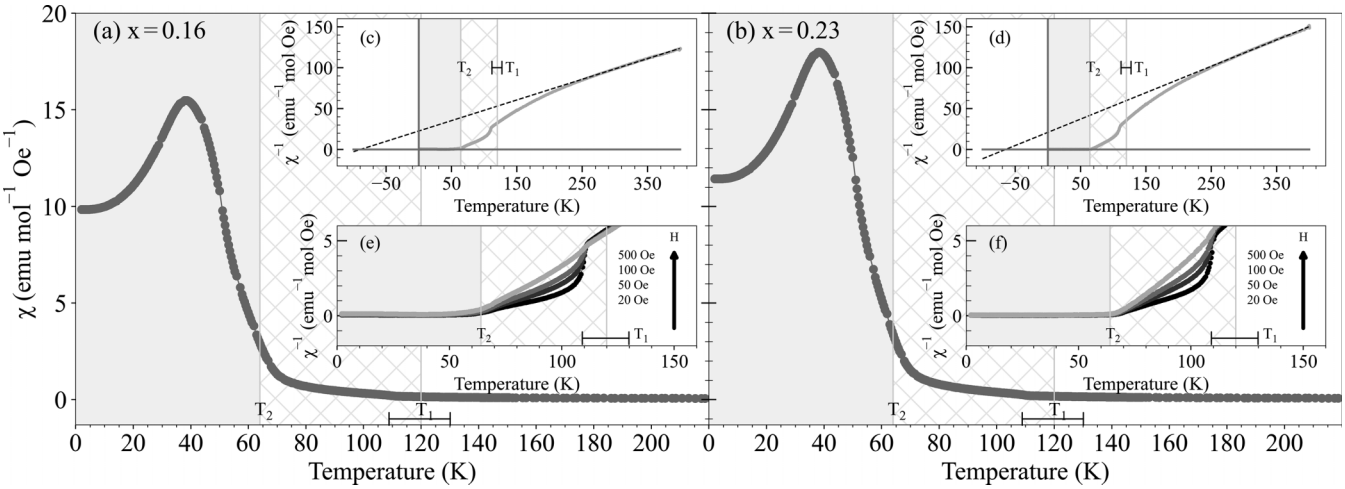

FIG. 5. Temperature dependence of the FCC susceptibility under an applied field of 100 Oe for (a) the $x = 0.16$ sample and (b) the $x = 0.23$ sample. FCC inverse susceptibility measurements collected under 100 Oe field with a Curie-Weiss fit of the 400–250-K data shown by the dotted line for (c) the $x = 0.16$ sample and (d) the $x = 0.23$ sample. FCC inverse susceptibility measurements under different applied DC fields for (e) the $x = 0.16$ sample and (f) the $x = 0.23$ sample. The gray solid and hatched regions correspond to the temperature regions $T < T_2$ and $T_2 \leqslant T \leqslant T_1$. The uncertainty on T_1 is indicated by a horizontal error bar.

This is widely regarded in the literature to be characteristic of a Griffiths phase consisting of ferromagnetic clusters [1,16,27]. However, since our experimental results indicate that only antiferromagnetic clusters are present in this temperature region, which intuitively cannot cause a downturn to the inverse susceptibility, this feature is likely due to the presence of a FM or FIM impurity phase. The high-temperature high-pressure synthesis of the $A_2A'A''Mn_4O_{12}$ manganites is susceptible to the formation of impurities, such as the orthorhombic $R_{0.667}Mn_{0.333}MnO_3$ manganites, which have ordering temperatures between 105 and 110 K and are expected to order ferromagnetically or ferrimagnetically [28]. While there are no diffraction peaks in the NPD pattern that would be consistent with a $Y_{0.67}Mn_{0.33}MnO_3$ impurity, we note that magnetometry measurements can be more sensitive to the presence of such impurities than diffraction. Below T_2 the magnetic susceptibility rapidly increases, which is consistent with the onset of the long-range FIM ordering.

D. Discussion

In the simple perovskite manganites, $AMnO_3$, the magnetic structure immediately below T_N is determined by the superexchange interactions between Mn ions at the B sites; we refer to these as B-B interactions. The Goodenough-Kanamori-Anderson rules then provide a framework in which one can predict the sign and approximate strength of the B-B exchange, depending upon the orbital configuration of the Mn-O-Mn superexchange pathways. Applying the same rules to the B-B exchange interactions in the columnar ordered quadruple perovskites one predicts an AFM B-site structure composed of A_iA_i modes. However, in all previously studied columnar ordered perovskites [19–21] ferromagnetic modes are found on the B sites, and together with the A sites these materials adopt a ferrimagnetic structure. A key difference between the simple and quadruple perovskites is the presence of magnetic transition metal ions at the A sites (A' and A'' sites in the perfectly ordered columnar systems), and it was suggested that ferromagnetism at the B sites in the columnar ordered systems is stabilized by A-B exchange interactions dominating B-B interactions. This frustration between A-B and B-B exchange has manifested in reduced ordered moments [20] and large spin canting [21].

Here, in $[Y_{2-x}Mn_x]Mn_6O_{12}$, we have observed an example of an AFM A_iA_i B-site magnetic structure in the quadruple perovskites, which emerges as a separate, poorly correlated phase that competes with the typical ferrimagnetic long-range order. Note that we can rule out the scenario of spin canting within a single phase as both F and A modes are polarized in the same direction (z). The AFM phase appears at a higher temperature than the FIM phase, likely due to the effects of frustration in the FIM case. This is consistent with symmetry; the A sites do not enter into the Γ_1^+ irreducible representation by which the B-site $AzAz$ modes transform. Hence, for $AzAz$ ordering at the B sites the A-B exchange interactions exactly cancel by symmetry. In contrast, a net A-B exchange is allowed within the Γ_2^+ symmetry of the ferrimagnetic phase, which will compete with the B-B interactions.

We propose that the observed phase separation is driven by inhomogeneities in the sample, such that in minority regions B-B exchange wins over A-B interactions allowing B-site AFM clusters to develop. In the $x = 0.23$ sample 11.5(5)% of the Y sites are occupied by Mn, and in the $x = 0.16$ sample 8.0(4)% of the Y sites are occupied by Mn. This local substitution of nonmagnetic Y by magnetic Mn can be considered *spin doping* of the A-site sublattice, which will tune the competition between A-B and B-B exchange in favor of the FIM structure. Inhomogeneities in the amount of spin doping can then give rise to AFM/FIM phase separation, whereby clusters of antiferromagnetic order form in regions of the crystal where there is minimal substitutional disorder on the A sites. This scenario naturally explains the

larger AFM phase fraction found for $x = 0.16$ (less spin doping) compared to $x = 0.23$ (more spin doping), as shown in Fig. 4.

Finally, we comment on the suppression of the FIM phase in favor of the AFM phase at low temperature, an effect that is enhanced in the lower spin-doped $x = 0.16$ sample. We assume that the changes in average magnetic intensity observed in the NPD experiments reflect a change in phase fraction, as a reduction in the FIM moment on cooling would be unphysical for this insulating system. The observed changes in the average intensity scattered from the AFM/FIM phases, reflective of the changing phase fractions, implies that the average competition between *A*-*B* and *B*-*B* exchange has been tuned by temperature. The ratio of *A*-*B* to *B*-*B* exchange will change in line with the changing ratio of the *A*- and *B*-site magnetic moments, such that at a certain temperature regions of the crystal with a critical concentration of spin doping could switch from being FIM to being AFM.

IV. CONCLUSIONS

In conclusion, our results demonstrate that the $[Y_{2-x}Mn_x]Mn_6O_{12}$ quadruple perovskite manganites can support an inhomogeneous distribution of competing exchange interactions, owing to a substitution of magnetic Mn ions onto a three-dimensional framework of nonmagnetic Y. In regions where the nominal stoichiometry is retained (i.e., $x \approx 0$), *A*-*B* interactions are minimized on average, giving rise to short-range antiferromagnetic clusters within the typical well-correlated ferrimagnetic order. Our results suggest that spin doping may have a profound impact on the nature of magnetic phases stabilized in the presence of competing exchange between multiple magnetic sublattices often found in transition metal oxides. In future studies it would be of interest to quantify the relationship between the substitutional disorder and size and extent of the antiferromagnetic clusters, which would enhance our understanding of the physical properties of disordered magnetic systems. Furthermore, one could explore emergent material properties associated with the disordered state and controlled through spin doping, analogous to the Griffiths type phases stabilized through charge degrees of freedom.

ACKNOWLEDGMENTS

A.A.B. and K.Y. acknowledge support from a Grant-in-Aid for Scientific Research from the Japan Society for the Promotion of Science (Grant No. JP22H04601) and from the Kazuchika Okura Memorial Foundation (Grant No. 2022-11). The International Center for Materials Nanoarchitectonics (MANA) is supported by World Premier International Research Center Initiative, Ministry of Education, Culture, Sports, Science, and Technology, Japan.

APPENDIX

1. Crystal structure parameters

In the $x = 0.23$ sample 13.2(4)% of Y1 sites and 10.0(4)% of Y2 sites were occupied by Mn ions, and the remainder were occupied by Y. In the $x = 0.16$ sample 10.0(4)% of Y1 sites and 6.0(4)% of Y2 sites were occupied by Mn ions, and the remainder were occupied by Y. Both samples contained a YMn_2O_5 impurity, with a weight fraction of 1.26 and 1.32 wt. % respectively. The $x = 0.16$ sample also contained a $YMnO_3$ impurity, with a weight fraction of 0.37 wt. %. An excellent fit was achieved for both samples, $R = 3.30\%$, $wR = 3.30\%$, and $R_{\text{Bragg}} = 3.04\%$ for the $x = 0.23$ sample at 250 K and $R = 3.36\%$, $wR = 3.71\%$, and $R_{\text{Bragg}} = 3.02\%$ for the $x = 0.16$ sample at 255 K. The refined crystal structure parameters for each sample are given in Tables III and IV.

2. Magnetic symmetry

a. Magnetic modes

Symmetry-adapted modes that constitute candidate magnetic structures for all ordered phases of $[Y_{2-x}Mn_x]Mn_6O_{12}$

TABLE III. Crystal structure parameters of $x = 0.23$ ($Z = 4$, space group *Pmmn*) refined at 255 K. The lattice parameters were determined to be $a = 7.247\,42(7)$ Å, $b = 7.434\,00(2)$ Å, and $c = 7.788\,94(9)$ Å. Excellent reliability parameters of $R = 3.30\%$, $wR = 3.30\%$, and $R_{\text{Bragg}} = 3.04\%$ were achieved in the refinement. Bond valence sums (BVS) were calculated using the bond valence parameters, $R_0(Y^{3+}) = 2.01(1)$, $R_0(Mn^{3+}) = 1.76(1)$, $R_0(Mn^{2+}) = 1.79(1)$, $R_0(Mn^{3+}) = 1.76(1)$, $R_0(Mn^{4+}) = 1.75(1)$, and $B = 0.37$ [29]. The occupation factor for each of the symmetry inequivalent sites is given in the last column. Note the Y sites are occupied by both Y and Mn, where only the occupation by Y is listed in the table. The total occupation for the Y sites is 0.25, and thus the Mn occupation on the Y1 and Y2 sites is 0.033 and 0.025, respectively.

Atom	Site	x	y	z	U_{iso} (Å^2)	BVS ($\|e\|$)	Occ.
Y1	2*a*	0.25	0.25	0.7816(4)	0.0067(1)	2.92(5)	0.217(1)
Y2	2*a*	0.25	0.25	0.2839(4)	0.011(2)	2.88(8)	0.225(1)
Mn1	2*b*	0.75	0.25	0.7227(6)	0.002(1)	2.70(5)	0.25
Mn2	2*b*	0.75	0.25	0.2393(8)	0.019(5)	1.96(6)	0.25
Mn3	4*c*	0	0	0	0.002(1)	3.16(9)	0.5
Mn4	4*d*	0	0	0.5	0.09(1)	3.6(1)	0.5
O1	8*g*	0.4349(2)	−0.0682(2)	0.2673(2)	0.0111(6)		1.0
O2	4*f*	0.0568(3)	0.25	0.0422(3)	0.0105(7)		0.5
O3	4*e*	0.25	0.5296(3)	0.9220(3)	0.0087(7)		0.5
O4	4*f*	0.5417(3)	0.25	0.4159(3)	0.0109(7)		0.5
O5	4*e*	0.25	0.4338(3)	0.5403(3)	0.0095(7)		0.5

TABLE IV. Crystal structure parameters of $x = 0.16$ ($Z = 4$, space group *Pmmn*) refined at 250 K. The lattice parameters were determined to be $a = 7.252\,84(8)$ Å, $b = 7.448\,42(8)$ Å, and $c = 7.7963(1)$ Å. Excellent reliability parameters of $R = 3.49\%$, $wR = 3.79\%$, and $R_{\text{Bragg}} = 3.14\%$ were achieved in the refinement. Bond valence sums (BVS) were calculated using the bond valence parameters, $R_0(Y^{3+}) = 2.01(1)$, $R_0(Mn^{3+}) = 1.76(1)$, $R_0(Mn^{2+}) = 1.79(1)$, $R_0(Mn^{3+}) = 1.76(1)$, $R_0(Mn^{4+}) = 1.75(1)$, and $B = 0.37$ [29]. The occupation factor for each of the symmetry inequivalent sites is given in the last column. Note the Y sites are occupied by both Y and Mn, where only the occupation by Y is listed in the table. The total occupation for the Y sites is 0.25, and thus the Mn occupation on the Y1 and Y2 sites is 0.024 and 0.015, respectively.

Atom	Site	x	y	z	U_{iso} (Å^2)	BVS ($\|e\|$)	Occ.
Y1	2*a*	0.25	0.25	0.7814(4)	0.0120(9)	2.91(5)	0.226(1)
Y2	2*a*	0.25	0.25	0.284(4)	0.0081(9)	2.89(5)	0.235(1)
Mn1	2*b*	0.75	0.25	0.7246(7)	0.004(1)	2.66(5)	0.25
Mn2	2*b*	0.75	0.25	0.2402(1)	0.033(2)	1.93(6)	0.25
Mn3	4*c*	0	0	0	0.0076(1)	3.2(1)	0.5
Mn4	4*d*	0	0	0.5	0.0074(1)	3.5(1)	0.5
O1	8*g*	0.4352(2)	−0.0677(2)	0.2667(2)	0.0126(6)		1.0
O2	4*f*	0.0570(3)	0.25	0.0415(3)	0.0111(7)		0.5
O3	4*e*	0.25	0.5291(3)	0.9223(3)	0.0089(8)		0.5
O4	4*f*	0.5401(3)	0.25	0.4148(3)	0.0126(8)		0.5
O5	4*e*	0.25	0.4334(3)	0.5399(3)	0.0097(7)		0.5

are given below. We define four modes, F_i, A_i, X_i, and Y_i, that span the four symmetry equivalent *B*-site Mn ions of a given Mn3 ($z = 0$) or Mn4 ($z = 1/2$) layer in a single *Pmmn* unit cell (the subscript $i = x,\ y,$ or z denotes the direction of the moment component, where $x||a$, $y||b$, and $z||c$), adopting the same labeling scheme as established for other members of the columnar ordered quadruple perovskites [21]. The magnetic order of a single layer is then described by a linear combination of these modes. For each mode the relative signs of the magnetic moment components on each of the four sites are given in Table V. We note that, under the physical constraint that every symmetry equivalent magnetic ion has the same size magnetic moment, combined modes must have orthogonal magnetic moment components.

As for the *A* sites, we define two modes, F_i and A_i, that span the two symmetry equivalent *A*-site ions of a *R*1, *R*2, Mn1, or Mn2 sublattice in a single *Pmmn* unit cell. The relative signs of the magnetic moment components on each of the two sites are given in Table VI.

b. Symmetry analysis

The NPD experiments described in Sec. III A demonstrate a Γ-point propagation vector for all the magnetically ordered phases of $[Y_{2-x}Mn_x]Mn_6O_{12}$. Symmetry analysis was performed using ISODISTORT [30], taking the *Pmmn* structure detailed in Appendix 1 as the parent. The magnetic Γ representation for the Wyckoff positions describing magnetic sites of the $[Y_{2-x}Mn_x]Mn_6O_{12}$ *Pmmn* crystal structure each decompose into seven irreducible representations, listed in Table VII, and described in terms of the symmetry adapted basis modes defined above.

TABLE V. Magnetic modes that span the four symmetry equivalent *B*-site Mn ions of a Mn3 ($z = 0$) or Mn4 ($z = 1/2$) layer in a single *Pmmn* unit cell. The subscript i denotes the direction of the moment component.

Fractional coordinates	F_i	A_i	X_i	Y_i
0.0, 0,0, z	+	+	+	+
0.5, 0.0, z	+	−	−	+
0.0, 0.5, z	+	−	+	−
0.5, 0.5, z	+	+	−	−

c. Structure factor calculations

To simplify the structure factor calculations of the *A* sites, they are approximated to have z fractional coordinates of exactly 1/4 or 3/4. From these calculations, Eqs. (A1) and (A2), one can see that the F_i mode has finite intensity for reflections where $h + k + l$ is even and zero intensity for reflections where $h + k + l$ is odd. In contrast the A_i mode has finite intensity for reflections where $h + k + l$ is odd, and zero intensity for reflections where $h + k + l$ is even. The presence of broad diffuse intensity about the {110} and {112} families of reflections, and the absence of any broad diffuse intensity about the {2,0,0} family, is only consistent with the Mn1 and Mn2 sublattices ordering with F_i modes where the Mn1 and Mn2 sublattices are coupled antiferromagnetically. In the FIM phase the Mn1 and Mn2 sublattices do order with F_i modes that are coupled antiferromagnetically, hence it is unlikely that this could be a competing magnetic phase to the FIM order. Furthermore if the broad diffuse intensity originated in F_i *A*-site modes coupled antiferromagnetically, one may expect that as the long-range FIM order develops, the broad

TABLE VI. Magnetic modes that span the two symmetry equivalent *A*-site ions of a *R*1, *R*2, Cu1, or Mn2 sublattice in a single *Pmmn* unit cell. The subscript i denotes the direction of the moment component.

Fractional coordinates	F_i	A_i
x, y, z	+	+
$x + 1/2, y + 1/2, z + 1/2$	+	−

TABLE VII. The magnetic Γ-point irreducible representations described for each of the symmetry inequivalent magnetic sites of the $[Y_{2-x}Mn_x]Mn_6O_{12}$ *Pmmn* $A_2A'A''B_4O_{12}$ crystal structure using the symmetry adapted basis modes defined above, for $k = (0, 0, 0)$.

Irrep.	Y1	Y2	Mn1	Mn2	Mn3	Mn4
Γ_1^+					Y_x, X_y, A_z	Y_x, X_y, A_z
Γ_2^+	F_z	F_z	F_z	F_z	X_x, Y_y, F_z	X_x, Y_y, F_z
Γ_3^+	F_x	F_x	F_x	F_x	F_x, A_y, X_z	F_x, A_y, X_z
Γ_4^+	F_y	F_y	F_y	F_y	A_x, F_y, Y_z	A_x, F_y, Y_z
Γ_1^-	A_z	A_z	A_z	A_z		
Γ_3^-	A_y	A_y	A_y	A_y		
Γ_4^-	A_x	A_x	A_x	A_x		

diffuse intensity should shift into the sharp magnetic Bragg peaks. However, the broad diffuse intensity *grows* below T_2, and at the expense of the sharp magnetic Bragg peaks below ≈33 K.

For the F_i *A-site mode*, we have

$$F_{(h,k,l)} = f_{\mathrm{Mn1}}(e^{\pi ik} + e^{\pi i(h+l)}) + f_{\mathrm{Mn2}}(e^{\pi i(h)} + e^{\pi i(k+l)}), \tag{A1}$$

and for A_i we have

$$F_{(h,k,l)} = f_{\mathrm{Mn1}}(\exp^{\pi ik} - \exp^{\pi i(h+l)}) + f_{\mathrm{Mn2}}(\exp^{\pi i(h)} - \exp^{\pi i(k+l)}). \tag{A2}$$

The structure factor equations for each of the symmetry adapted *B*-site ion basis modes are given by Eqs. (A3)–(A6). Structure factor equations taking into account two *B*-site magnetic modes that describe the magnetic structure of the *B* sites on the $z = 0$ layer (the first mode listed) and the $z = 1/2$ layer (the second mode listed) are given by Eqs. (A7)–(A14), where the moment magnitudes across the two sublattices are constrained to be the same, and they are assumed to have the same form factor for simplicity.

For the F_i *B-site mode*, we have

$$F_{(h,k,l)} = f_m(1 + e^{\pi ih} + e^{\pi ik} + e^{\pi i(h+k)}), \tag{A3}$$

for A_i we have

$$F_{(h,k,l)} = f_m(1 - e^{\pi ih} - e^{\pi ik} + e^{\pi i(h+k)}), \tag{A4}$$

for X_i we have

$$F_{(h,k,l)} = f_m(1 - e^{\pi ih} + e^{\pi ik} - e^{\pi i(h+k)}), \tag{A5}$$

for Y_i we have

$$F_{(h,k,l)} = f_m(1 + e^{\pi ih} - e^{\pi ik} - e^{\pi i(h+k)}), \tag{A6}$$

for F_iF_i we have

$$F_{(h,k,l)} = f_m(1 + e^{\pi ih} + e^{\pi ik} + e^{\pi i(h+k)} + e^{\pi il} + e^{\pi i(h+l)} + e^{\pi i(k+l)} + e^{\pi i(h+k+l)}), \tag{A7}$$

for $F_iF_{\bar{i}}$ we have

$$F_{(h,k,l)} = f_m(1 + e^{\pi ih} + e^{\pi ik} + e^{\pi i(h+k)} - e^{\pi il} - e^{\pi i(h+l)} - e^{\pi i(k+l)} - e^{\pi i(h+k+l)}), \tag{A8}$$

for A_iA_i we have

$$F_{(h,k,l)} = f_m(1 - e^{\pi ih} - e^{\pi ik} + e^{\pi i(h+k)} + e^{\pi il} - e^{\pi i(h+l)} - e^{\pi i(k+l)} + e^{\pi i(h+k+l)}), \tag{A9}$$

for $A_iA_{\bar{i}}$ we have

$$F_{(h,k,l)} = f_m(1 - e^{\pi ih} - e^{\pi ik} + e^{\pi i(h+k)} - e^{\pi il} + e^{\pi i(h+l)} + e^{\pi i(k+l)} - e^{\pi i(h+k+l)}), \tag{A10}$$

for X_iX_i we have

$$F_{(h,k,l)} = f_m(1 - e^{\pi ih} + e^{\pi ik} - e^{\pi i(h+k)} + e^{\pi il} - e^{\pi i(h+l)} + e^{\pi i(k+l)} - e^{\pi i(h+k+l)}), \tag{A11}$$

for $X_iX_{\bar{i}}$ we have

$$F_{(h,k,l)} = f_m(1 - e^{\pi ih} + e^{\pi ik} - e^{\pi i(h+k)} - e^{\pi il} + e^{\pi i(h+l)} - e^{\pi i(k+l)} + e^{\pi i(h+k+l)}), \tag{A12}$$

for Y_iY_i we have

$$F_{(h,k,l)} = f_m(1 + e^{\pi ih} - e^{\pi ik} - e^{\pi i(h+k)} + e^{\pi il} + e^{\pi i(h+l)} - e^{\pi i(k+l)} - e^{\pi i(h+k+l)}), \tag{A13}$$

and for $Y_iY_{\bar{i}}$ we have

$$F_{(h,k,l)} = f_m(1 + e^{\pi ih} - e^{\pi ik} - e^{\pi i(h+k)} - e^{\pi il} - e^{\pi i(h+l)} + e^{\pi i(k+l)} + e^{\pi i(h+k+l)}). \tag{A14}$$

3. Diffuse scattering

Here we include an analysis of the diffuse scattering centered about the (110) family of reflections as a function of temperature, as shown in Fig. 6.

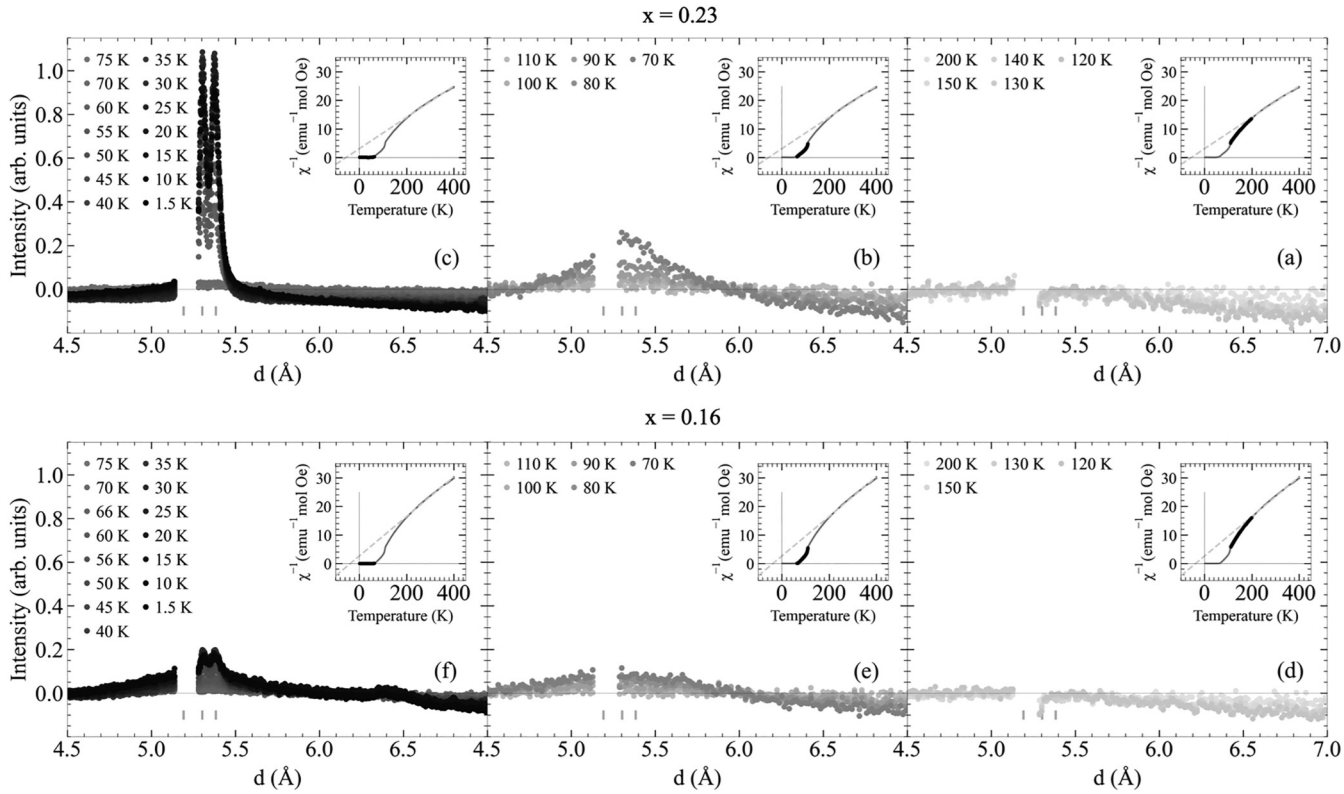

FIG. 6. Neutron powder-diffraction patterns collected on WISH centered about the (110) family of reflections. Data collected on the $x = 0.23$ sample between (a) 120 and 200 K subtracted from 250-K data, (b) 70 and 110 K subtracted from 120-K data, and (c) 1.5 and 75 K subtracted from 85-K data. Data collected on the $x = 0.16$ sample between (d) 120 and 200 K subtracted from 255-K data, (e) 70 and 110 K subtracted from 120-K data, and (f) 1.5 and 75 K subtracted from 100-K data. The insets show the temperature dependence of FCC magnetization measurements under an applied DC field of 100 Oe for each of the samples, with the temperature range of the corresponding neutron powder-diffraction data emphasized in bold. A Curie-Weiss fit of the inverse susceptibility for 400–200-K data is given by the dashed line.

4. SANS

Magnetic SANS intensities collected under applied magnetic fields of 0.01, 0.1, and 0.5 T at 5, 90, and 130 K for the $x = 0.23$ sample are shown in Fig. 7.

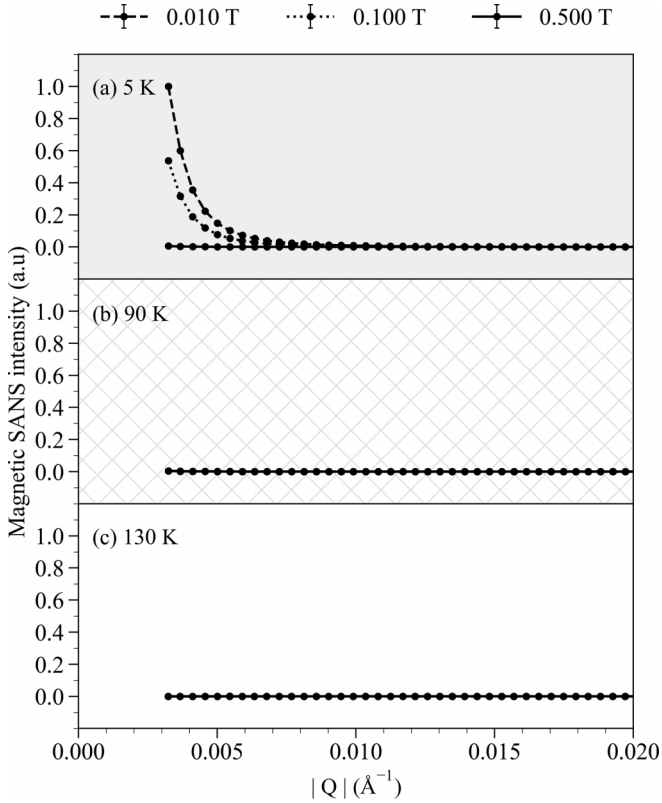

FIG. 7. Normalized magnetic SANS intensity under different applied magnetic fields at (a) 5 K, (b) 90 K, and (c) 130 K for the $x = 0.23$ sample.

5. Specific heat capacity measurements

Specific heat data measured on both samples at two different fields are shown in Fig. 8. Only a single phase transition, characteristic of the ordering of the FIM phase, is observed in both samples.

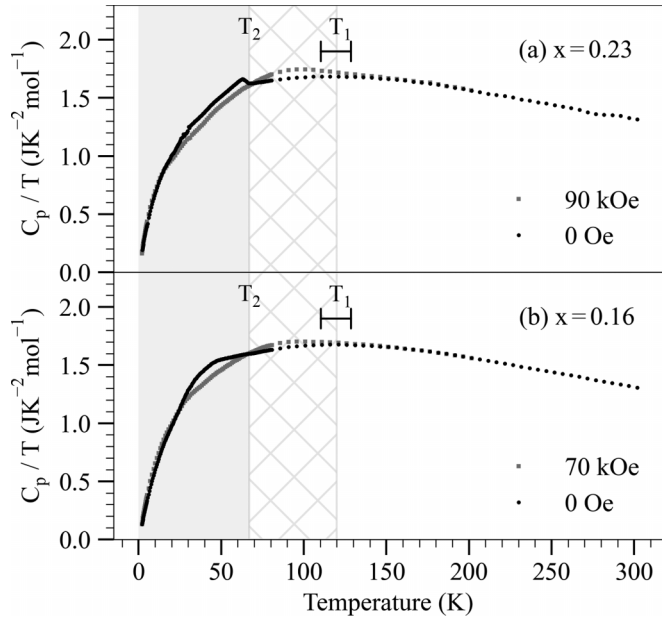

FIG. 8. Specific heat data shown for the (a) $x = 0.23$ and (b) the $x = 0.16$ $[Y_{2-x}Mn_x]Mn_6O_{12}$ samples.

[1] C. Magen, P. A. Algarabel, L. Morellon, J. P. Araújo, C. Ritter, M. R. Ibarra, A. M. Pereira, and J. B. Sousa, Phys. Rev. Lett. **96**, 167201 (2006).

[2] R. B. Griffiths, Phys. Rev. Lett. **23**, 17 (1969).

[3] A. J. Bray and M. A. Moore, J. Phys. C **15**, L765 (1982).

[4] A. J. Bray, Phys. Rev. Lett. **59**, 586 (1987).

[5] P. W. Anderson, Phys. Today **43**, 9 (1990).

[6] E. Dagotto, Science **309**, 257 (2005).

[7] C. Zener, Phys. Rev. **82**, 403 (1951).

[8] J. W. Lynn, R. W. Erwin, J. A. Borchers, Q. Huang, A. Santoro, J.-L. Peng, and Z. Y. Li, Phys. Rev. Lett. **76**, 4046 (1996).

[9] J. M. De Teresa, M. Ibarra, P. Algarabel, C. Ritter, C. Marquina, J. Blasco, J. Garcia, A. del Moral, and Z. Arnold, Nature (London) **386**, 256 (1997).

[10] M. Uehara, S. Mori, C. Chen, and S.-W. Cheong, Nature (London) **399**, 560 (1999).

[11] D. E. Cox, P. G. Radaelli, M. Marezio, and S.-W. Cheong, Phys. Rev. B **57**, 3305 (1998).

[12] J. B. Goodenough, *Magnetism and the Chemical Bond*, edited by F. A. Cotton (Wiley, New York, 1963).

[13] R. D. Merithew, M. B. Weissman, F. M. Hess, P. Spradling, E. R. Nowak, J. O'Donnell, J. N. Eckstein, Y. Tokura, and Y. Tomioka, Phys. Rev. Lett. **84**, 3442 (2000).

[14] J. Burgy, M. Mayr, V. Martin-Mayor, A. Moreo, and E. Dagotto, Phys. Rev. Lett. **87**, 277202 (2001).

[15] J. M. De Teresa, M. R. Ibarra, P. Algarabel, L. Morellon, B. García-Landa, C. Marquina, C. Ritter, A. Maignan, C. Martin, B. Raveau, A. Kurbakov, and V. Trounov, Phys. Rev. B **65**, 100403(R) (2002).

[16] M. B. Salamon, P. Lin, and S. H. Chun, Phys. Rev. Lett. **88**, 197203 (2002).

[17] V. B. Shenoy, T. Gupta, H. R. Krishnamurthy, and T. V. Ramakrishnan, Phys. Rev. Lett. **98**, 097201 (2007).

[18] W. Jiang, X.Z. Zhou, G. Williams, Y. Mukovskii, and K. Glazyrin, Phys. Rev. Lett. **99**, 177203 (2007).

[19] A. M. Vibhakar, D. D. Khalyavin, P. Manuel, L. Zhang, K. Yamaura, P. G. Radaelli, A. A. Belik, and R. D. Johnson, Phys. Rev. B **99**, 104424 (2019).

[20] A. M. Vibhakar, D. D. Khalyavin, P. Manuel, R. Liu, K. Yamaura, A. A. Belik, and R. D. Johnson, Phys. Rev. B **102**, 214428 (2020).

[21] A. M. Vibhakar, D. D. Khalyavin, P. Manuel, J. Liu, A. A. Belik, and R. D. Johnson, Phys. Rev. Lett. **124**, 127201 (2020).

[22] L. Zhang, Y. Matsushita, K. Yamaura, and A. A. Belik, Inorg. Chem. **56**, 5210 (2017).

[23] L. C. Chapon, P. Manuel, P. G. Radaelli, C. Benson, L. Perrott, S. Ansell, N. J. Rhodes, D. Raspino, D. Duxbury, E. Spill, and J. Norris, Neutron News **22**, 22 (2011).

[24] We cannot distinguish as to whether homovalent or heterovalent substitution occurs, i.e., if it is Mn^{3+} or Mn^{2+} that substitutes Y^{3+} on the *A* sites. Hence it is possible that in addition to spin doping, charge doping may also occur. However, as these samples remain insulating [22], in comparison to the simple perovskite manganites where charge doping can induce a metal to insulator phase transition, we suggest that the changes we observe to the magnetic properties of these systems can largely be attributed to the effect of changing the spin properties of the *A*-site ions.

[25] A single A_i mode, i.e., on a single *B*-site layer, could also give rise to scattering on the (110) and (112), however significant intensity is also expected on the (111) reflection which was not observed.

[26] D. Billington, D. Ernsting, T. E. Millichamp, C. Lester, S. B. Dugdale, D. Kersh, J. A. Duffy, S. R. Giblin, J. W. Taylor, P. Manuel *et al.*, Sci. Rep. **5**, 12428 (2015).

[27] Z. W. Ouyang, V. K. Pecharsky, K. A. Gschneidner, D. L. Schlagel, and T. A. Lograsso, Phys. Rev. B **74**, 094404 (2006).

[28] L. Zhang, D. Gerlach, A. Dönni, T. Chikyow, Y. Katsuya, M. Tanaka, S. Ueda, K. Yamaura, and A. A. Belik, Inorg. Chem. **57**, 2773 (2018).

[29] N. E. Brese and M. O'Keeffe, Acta Crystallogr. Sect. B **47**, 192 (1991).

[30] B. J. Campbell, H. T. Stokes, D. E. Tanner, and D. M. Hatch, J. Appl. Crystallogr. **39**, 607 (2006).